Application of the Onsager variational principle to the power-law scaling for solid-state dewetting

Wei Jiang[1,2], Sisheng Wang[1] and Xianmin Xu[3*]

[1]School of Mathematics and Statistics, Wuhan University, Wuhan 430072, China

[2]Shenzhen Research Institute of Wuhan University, Shenzhen, 518057, China

[3]State Key Laboratory of Mathematical Sciences, NCMIS, Academy of Mathematics and Systems Science, Chinese Academy of Sciences, Beijing, 100190, China

May 18, 2026

Abstract

We examine the kinetics of surface diffusion-controlled, solid-state dewetting by consideration of the retraction of the contact in a semi-infinite solid thin film on a flat rigid substrate. The analysis is performed within the framework of the Onsager variational principle (OVP) applied to the surface diffusion-controlled morphology evolution. Based on this approach, we derive a simple, reduced-order model to quantitatively analyse the power-law scaling of the dewetting process. Using asymptotic analysis and numerical simulations for the reduced-order model, we find that the retraction distance grows as the 2/5 power of time and the height of the ridge, adjacent to the contact, grows as the 1/5 power of time for late time. While the asymptotic analysis focuses on late time and a relatively simple geometric model, the Onsager approach is applicable to all times and descriptions of the morphology of arbitrary complexity. To see this more clearly, we present another discrete model based on the OVP for simulating the solid-state dewetting problem. Numerical results show that both the thin film profile and the power-law behavior can be calculated correctly by the discrete model.

Keywords: solid-state dewetting, surface diffusion, Onsager variational principle, reduced model, power law scaling. 68.03.Cd, 68.35.-p, 68.35.Fx

1. Introduction

Solid-state dewetting of thin films on substrates has been observed in a wide range of systems by many research groups over many decades [1–8]. While solid-state dewetting is deleterious, in the sense that it leads to the destabilization/agglomeration of continuous deposited films, it can also be exploited to produce a controlled distribution of particles on a substrate. Recent examples include the formation of ordered arrays of nanoparticles and quantum dots, which have been exploited to produce sensors [9,10], optical and magnetic devices [9,11] and

*Corresponding author. E-mail:xmxu@lsec.cc.ac.cn

for catalysts for the growth of carbon and semiconductor nanotubes and nanowires [12,13]. Interest in such applications has driven research into the underlying mechanisms of solid-state dewetting [14–26].

In general, dewetting of thin solid films is similar in many aspects to the wetting/dewetting of liquid thin films [27]. However, a significant difference is that its mass transport is dominated by surface diffusion rather than fluid dynamics [19,21,26,28]. Owing to the characteristics of fluids, liquid dewetting is typically rapid in kinetic evolution and produces smooth morphologies, such as spherical-cap droplets, nearly circular holes, and continuous rounded rims. In contrast, solid-state dewetting proceeds comparatively slowly and the resulting morphologies are strongly influenced by crystallographic orientation, surface energy anisotropy and grain boundaries, which give rise to polygonal holes, faceted particles or isolated island [1,23,24]. Moreover, a typical morphological feature of surface diffusion-controlled solid-state dewetting is the formation of a thickened ridge followed by a valley at the retracting film edge, the amplitudes of which increase with time/retraction distance [4,15,16,29–31]. Experimental observations show that the edge retraction distance scales as the 2/5 power of time (at long time) [30,31]. While this power-law has been widely observed in numerical simulations of solid thin film dewetting [15,19,21], rigorous theoretical analysis has remained elusive (despite reasonable approximate solutions [22,32]).

Brandon and Bradshaw (referred to as the BB model here) presented a simple geometric model for analysing this problem more than half a century ago [32]. Based on the observation that edge retraction and ridge growth are the main hallmarks of surface diffusion-controlled solid state dewetting in experiments, BB described the cross-sectional profile of the discontinuous film as a semicircle that hits the substrate at the right contact angle (i.e., a contact angle of 90°) and connects with the film with a uniform thickness. With this simple profile, they obtained two important scaling laws: the radius of a growing hole increases with the 2/5 power of time, and the ridge height grows with the 1/5 power of time. The correspondence of these results with experimental observations demonstrate that this simple profile is sufficient to capture the essential features of surface diffusion-controlled solid-state dewetting.

Zucker *et al.* reexamined the BB model with the generalization that the cross-section of the profile needs not be semi-circular and the contact/Young angle θ_0 needs not be 90° (see Fig. 1). Their solution, for the mass-conserving (while the BB solution does not conserve the mass) surface diffusion-controlled dewetting, reproduces the 2/5 power-law [22,33] of the retracting distance in the long-time limit. However, their solution is both complicated and approximate.

The Onsager variational principle (OVP), first formulated in 1931 [34,35], is based on the reciprocal symmetry in linear irreversible thermodynamics. This variational principle has found wide application in deriving evolution equations in soft matter physics [36,37]. About ten years ago, Masao Doi first introduce the idea to use the OVP as an approximation tool in [38]. Later on the approach has been applied to derive reduced models in fluid dynamics [39–42]. This variational approach has also been applied to surface-diffusion controlled solid-state dewetting problems in [25,26]. Recently, the idea has been adopted to derive numerical methods for gradient flow systems in [43–47].

In this paper, we present a new approach for analyzing the power-law scaling of surface diffusion-controlled, solid-state dewetting that is both rigorous (conserving the total mass) and based upon the irreversible thermodynamics variational approach for surface diffusion-controlled morphology evolution problems [25,26]. While this

work builds on the earlier developments in the application of the OVP to surface diffusion-controlled, capillarity-driven morphology evolution [25,26], *this paper specifically: (1) addresses the non-trivial power-law scaling of solid-state dewetting, and (2) provides an example of how to apply the OVP to reduce the standard normal partial differential equations describing the morphology evolution to a set of ordinary differential equations that can be solved via asymptotic analysis and direct numerical solutions.*

This paper is organized as follows. In the next section, we briefly review the application of the OVP to construct a reduced-order model for an evolving, dissipative system. In Section 3, we apply this approach to the power-law retraction of the edge of a semi-infinite thin film on a substrate that results in an ordinary differential equation (ODE) for surface diffusion-controlled solid-state dewetting. In Section 4 and 5, we provide both asymptotic analysis and numerical simulations for the resulted ODE, and recover the 2/5 experimentally and simulation-observed power-law. In section 6, we introduce another dimensionless model based on the OVP, for simulating the solid state-dewetting problem. Finally, we draw some conclusions in Section 7.

2. The Onsager variational principle (OVP)

Consider an isothermal system that may include interfaces (e.g., the solid-vapor interface, solid-substrate interface, and vapor-substrate interface). If the system deviates from its equilibrium state, then there will be spontaneous processes that tend to bring the system back to equilibrium. In the linear response regime (i.e., not far from equilibrium), the time evolution of the system is governed by a variational principle. Let $\alpha(t) = (\alpha_1(t), \alpha_2(t), \ldots, \alpha_n(t))$ be a set of state variables. The time evolution of the system, may be described as the time derivatives of these state variables $\dot{\alpha}(t) = (\dot{\alpha}_1(t), \dot{\alpha}_2(t), \ldots, \dot{\alpha}_n(t))$ (a raised dot "$\cdot$" denotes a time derivative); it is determined by minimizing the "Rayleighian" $\mathcal{R}$ with respect to the rates $\{\dot{\alpha}_i\}$ [25,38,39,48]:

$$\mathcal{R}(\alpha, \dot{\alpha}) = \dot{W}(\alpha, \dot{\alpha}) + \Phi(\alpha, \dot{\alpha}). \tag{2.1}$$

Here, $W(\alpha) := W(\alpha_1, \alpha_2, \ldots, \alpha_n)$ represents the total free energy of the system (a state function) and $\dot{W}$ is the rate of change of W,

$$\dot{W}(\alpha, \dot{\alpha}) = \sum_i \frac{\partial W}{\partial \alpha_i} \dot{\alpha}_i. \tag{2.2}$$

$\Phi(\alpha, \dot{\alpha})$, in Eq. (2.1), is the free energy dissipation function; it is half the free energy dissipation rate. In the linear response regime, the dissipation function can be written as a quadratic function of the rates $\{\dot{\alpha}_i\}$; i.e.,

$$\Phi(\alpha, \dot{\alpha}) = \frac{1}{2} \sum_{i,j} \zeta_{ij}(\alpha) \dot{\alpha}_i \dot{\alpha}_j, \tag{2.3}$$

where the damping/friction coefficients ζ_{ij} form a symmetric, positive definite matrix. Minimizing the Rayleighian with respect to the rates $\{\dot{\alpha}_i\}$ yields a set of kinetic equations

$$\sum_j \zeta_{ij} \dot{\alpha}_j = -\frac{\partial W}{\partial \alpha_i}, \qquad i = 1, 2, \ldots, n. \tag{2.4}$$

This describes the force balance between the potential force $-\frac{\partial W}{\partial \alpha_i}$ and the dissipative force $\frac{\partial \Phi}{\partial \dot{\alpha}_i}$ (which is linear in the rates $\{\dot{\alpha}_i\}$). A simple calculation shows that the variational principle leads to $\dot{W} = -2\Phi$, which means Φ is half the rate of free energy dissipation, as asserted above. This variational principle for *isothermal* systems,

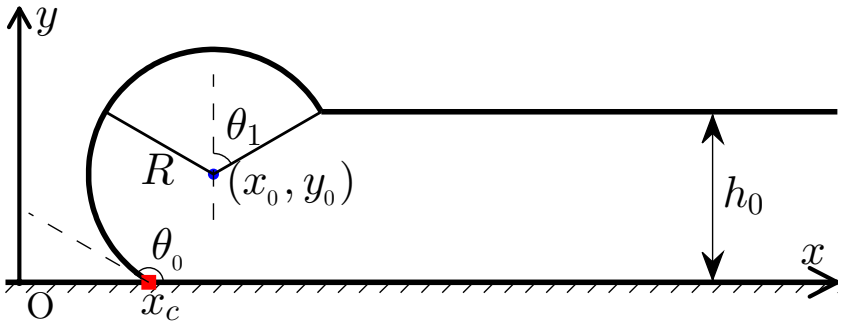

Figure 1: A schematic illustration of the model of the retracting contact and the correspond ridge. We assume that the profile of the film-vapor interface consists of a circular arc of radius $R := R(t)$ (center located at $(x_0(t), y_0(t))$), and a straight line representing the semi-infinite film of thickness h_0, measured from the substrate (i.e., the x-axis). The circular arc meets the substrate at the isotropic Young's angle θ_0. For convenience, all lengths are scaled by the film thickness.

outlined above, can be generalized to *non-isothermal* systems via the maximization of the Onsager-Machlup action [34,35].

The evolution of a dissipative system described by a set of field variables can be approximated by a *finite* set of slow variables. The total free energy W and dissipation function Φ can be obtained as functions of these state variables and their time derivatives. Application of the OVP then gives a system of *ordinary differential equations* (ODEs) that describes the time evolution of the slow variables, i.e., the time evolution of the system [38–40]. In the previous OVP to the surface diffusion-controlled, solid-state dewetting problem in [25], the objective is to analyse and simulate the evolution of the shrinkage velocity of solid toroidal island films on a substrate over time. In this paper, the thin film has a semi-infinite geometric shape and retracts along the substrate at a single contact point, and we investigate the power-law scaling of geometric quantities including the velocity of the moving contact point, the maximum and minimum heights of thin film. Different initial thin film geometric shapes shall lead to different questions of interest, although their evolution processes are driven by the surface diffusion and contact line migration. The field variables are chosen as a finite set of variables that represent a reduced-order description of the film profile. The purpose of the present work is to apply the OVP to the dynamics of solid-state dewetting. While it is possible to use this approach to accurately describe the evolution of the entire film profile, we focus here on deriving the power law of the retraction of the thin film dewetting front for which a relative simple description of the film profile suffices. We derive reduced models for the dynamics of a film with one contact point (as shown in Figure 1) by using the OVP, then perform asymptotic analysis and numerical simulations to derive the power law scaling of the retraction front in the long-time limit. We also derive a discrete model to simulate the evolution of the profile of the film.

3. A reduced-order variational model

We assume the film geometry with a retracting contact and ridge proposed by Zucker *et al.* [22], as shown in Fig. 1. We assume that the contact satisfies the isotropic Young's angle θ_0, i.e., $\cos\theta_0 = (\gamma_{VS} - \gamma_{FS})/\gamma_0$,

where γ_0, γ_{VS}, γ_{FS} represent the film-vapor, vapor-substrate and film-substrate interface energy per unit length. For simplicity in notations, we also introduce an angle $\theta_1(t)$ to characterize the position of the other end of the curve. We further assume that no free energy is dissipated by the motion of the contact point, i.e., no contact drag (this is consistent with the assumption that the contact angle always satisfies the equilibrium Young's angle condition).

In our application of the OVP, we focus on the reduced order model where the film profile is characterized by the parameters $R(t)$, $x_0(t)$, $y_0(t)$ and $\theta_1(t)$ that evolve during the dewetting process. These parameters are not independent; they satisfy several geometric constraints such that there is only one independent variable. Examination of the geometry of Fig. 1 shows that

$$\begin{cases} R\cos(\pi-\theta_0) &= y_0, \\ y_0 + R\cos\theta_1 &= h_0. \end{cases}$$

This implies that both y_0 and θ_1 can be written as functions of R. From these equations, we obtain

$$R(\cos\theta_1 - \cos\theta_0) = h_0. \tag{3.1}$$

Taking the time derivative of both sides of this equation, yields

$$(\cos\theta_1 - \cos\theta_0)\,\dot{R} = (R\sin\theta_1)\,\dot{\theta}_1, \tag{3.2}$$

which leads to

$$\dot{\theta}_1 = g_1(R,\theta_0,\theta_1)\,\dot{R}, \quad \text{where} \quad g_1(R,\theta_0,\theta_1) = \frac{\cos\theta_1 - \cos\theta_0}{R\sin\theta_1}. \tag{3.3}$$

Next, we consider the conservation of the film mass. The area $A := A(t)$ of the thin film enclosed by the circular arc and the rigid substrate is

$$A = \frac{1}{2}R^2(\theta_0+\theta_1) - \frac{1}{2}R^2\sin\theta_0\cos\theta_0 + \frac{1}{2}R^2\sin\theta_1\cos\theta_1 - R^2\cos\theta_0\sin\theta_1. \tag{3.4}$$

The mass/area conservation of thin film requires

$$\frac{\mathrm{d}A}{\mathrm{d}t} = \frac{\mathrm{d}}{\mathrm{d}t}\big[h_0(x_0 + R\sin\theta_1)\big], \tag{3.5}$$

where the area $h_0(x_0 + R\sin\theta_1)$ denotes the enclosed area of the right flat thin film part. According to the mass conservation (i.e., the area conservation of thin film), the increasing rate in the area enclosed by the left circular arc part is equal to the decreasing rate in the area of the right flat thin film part, as the contact point moves along the substrate from left to right. Inserting Eq. (3.4) into the above equation, we obtain a second important geometric relation

$$\begin{aligned} h_0\dot{x}_0 &= \Big[R\big(\theta_0+\theta_1 - \frac{1}{2}\sin 2\theta_0 + \frac{1}{2}\sin 2\theta_1 - 2\cos\theta_0\sin\theta_1\big) - h_0\sin\theta_1\Big]\dot{R} \\ &\quad + \Big[\frac{1}{2}R^2(1 - 2\cos\theta_0\cos\theta_1 + \cos 2\theta_1) - h_0 R\cos\theta_1\Big]\dot{\theta}_1. \end{aligned} \tag{3.6}$$

From the above relation, and making use of Eq. (3.3), we have

$$\dot{x}_0 = g_2\,\dot{R}, \tag{3.7}$$

where g_2 is given as

$$\begin{aligned} g_2 &= \Big[\frac{R}{h_0}\big(\theta_0+\theta_1-\frac{1}{2}\sin 2\theta_0+\frac{1}{2}\sin 2\theta_1-2\cos\theta_0\sin\theta_1\big)-\sin\theta_1\Big] \\ &\quad+\Big[\frac{R}{2h_0}(1-2\cos\theta_0\cos\theta_1+\cos 2\theta_1)-\cos\theta_1\Big]\frac{\cos\theta_1-\cos\theta_0}{\sin\theta_1}. \end{aligned}$$

Substituting Eq. (3.1) into this expression for g_2, we obtain g_2 as a function of θ_0 and θ_1,

$$g_2 := g_2(\theta_0,\theta_1) = \frac{1}{\cos\theta_1-\cos\theta_0}(\theta_0+\theta_1-\sin\theta_0\cos\theta_0-\sin\theta_1\cos\theta_0). \tag{3.8}$$

With the above geometrical relations in hand, we derive a reduced model for describing the dynamics of the dewetting process by application of the Onsager variational principle. We choose $R(t)$ as the only free variable. The total interfacial free energy of this system $W := W(t)$ can be written as

$$\begin{aligned} W =& W_1+W_2+W_3 \\ =&\gamma_0 R(\theta_0+\theta_1)-\gamma_0(x_0+R\sin\theta_1)+\gamma_0\cos\theta_0(x_0-R\sin\theta_0), \end{aligned} \tag{3.9}$$

where the first part $W_1=\gamma_0 R(\theta_1+\theta_0)$ denotes the interfacial free energy between the film and vapour phases on the circular part with surface energy density γ_0, where $R(\theta_1+\theta_0)$ denotes the length of arc length; the second part $W_2=-\gamma_0(x_0+R\sin\theta_1)$ is the interfacial free energy between the film-vapour phases on the right flat thin film part, and note here that we have taken away a constant thanks to the geometric set-up of the semi-infinite shape; the third part $W_3=\gamma_0\cos\theta_0(x_0-R\sin\theta_0)$ represents the interfacial free energy related with the flat rigid substrate.

Taking its time derivative and making use of Eqs. (3.3) and (3.7), we have

$$\begin{aligned} \dot{W} &= \frac{\partial W}{\partial R}\dot{R}+\frac{\partial W}{\partial\theta_1}\dot{\theta}_1+\frac{\partial W}{\partial x_0}\dot{x}_0 \\ &= \chi(R,\theta_0,\theta_1)\dot{R}, \end{aligned}$$

where $\dot{\theta}_1$ and $\dot{x}_0$ are replaced by using (3.3) and (3.7), and $\chi(R,\theta_0,\theta_1)$ is defined as

$$\chi(R,\theta_0,\theta_1)=\gamma_0\Big[(\theta_0+\theta_1-\sin\theta_1-\cos\theta_0\sin\theta_0)+R(1-\cos\theta_1)g_1-(1-\cos\theta_0)g_2\Big]. \tag{3.10}$$

Next, we compute the energy dissipation function for the evolving profile. For this, we parameterize the circular section of the film/vapor profile as

$$\begin{cases} x(\theta,t)=x_0(t)+R(t)\sin\theta, \\ y(\theta,t)=R(t)(\cos\theta-\cos\theta_0), \end{cases} \tag{3.11}$$

where $\theta\in[-\theta_0,\theta_1]$. The procedure for obtaining the dissipation function Φ is similar to that presented previously [25]. By taking the time derivative of the surface profile and multiplying by the surface unit normal vector $\mathbf{n}=(\sin\theta,\cos\theta)$, we obtain the normal velocity v_n of the circular section:

$$v_n(\theta)=\dot{x}_0\sin\theta+\dot{R}(1-\cos\theta_0\cos\theta),\quad \theta\in[-\theta_0,\theta_1]. \tag{3.12}$$

Based on the continuity equation for mass conservation which connects with j and v_n, i.e., $v_n + \partial_s j = 0$ [25], the corresponding (mass) flux $j := j(\theta)$, $\theta \in [-\theta_0, \theta_1]$ along the circular arc is

$$\begin{aligned} j(\theta) &= -\int_{-\theta_0}^{\theta} v_n(\theta) R \mathrm{d}\theta \\ &= R(\cos\theta - \cos\theta_0)\dot{x}_0 - R(\theta + \theta_0 - \sin\theta\cos\theta_0 - \sin\theta_0\cos\theta_0)\dot{R} \\ &= g_3(\theta, \theta_0, \theta_1) R\dot{R}, \end{aligned} \tag{3.13}$$

where

$$\begin{aligned} g_3(\theta, \theta_0, \theta_1) &= \Big[(\cos\theta - \cos\theta_0)\Big(\theta_0 + \theta_1 - (\sin\theta_0 + \sin\theta_1)\cos\theta_0\Big) \\ &\quad -(\cos\theta_1 - \cos\theta_0)\Big(\theta + \theta_0 - (\sin\theta + \sin\theta_0)\cos\theta_0\Big)\Big]\frac{1}{\cos\theta_1 - \cos\theta_0}. \end{aligned} \tag{3.14}$$

Here, we employed Eqs. (3.7) and (3.8) and imposed the zero-mass flux boundary condition at the contact point $j(-\theta_0) = 0$ (this implies that the total area/mass is conserved during the evolution) [21,25].

The dissipation function Φ can be written as [25]

$$\Phi = \frac{1}{2}\frac{k_B T}{D_s \nu \Omega_0^2}\int_{-\theta_0}^{\theta_1} j^2(\theta) R \,\mathrm{d}\theta, \tag{3.15}$$

where D_s is the surface diffusivity, ν is the number of diffusing atoms per unit area, Ω_0 is the atomic volume, and $k_B T$ is the thermal energy. By inserting (3.13) into this expression and making use of (3.7), it can be recast into the following quadratic form with respect to the rate function $\dot{R}$

$$\Phi := \Phi(R, \dot{R}) = \frac{1}{2}\zeta(R, \theta_0, \theta_1)\dot{R}^2, \tag{3.16}$$

where the friction coefficient $\zeta := \zeta(R, \theta_0, \theta_1)$ is

$$\zeta(R, \theta_0, \theta_1) = \frac{k_B T}{D_s \nu \Omega_0^2} R^3 \int_{-\theta_0}^{\theta_1} g_3(\theta, \theta_0, \theta_1)^2 \,\mathrm{d}\theta. \tag{3.17}$$

Applying the OVP [25,37], we write the Rayleighian of our system in terms of the free energy $W := W(R)$ and dissipation function $\Phi := \Phi(R, \dot{R})$:

$$\mathcal{R}(R, \dot{R}) = \dot{W} + \Phi. \tag{3.18}$$

Minimization of the Rayleighian $\mathcal{R}$ with respect to the rate variable $\dot{R}$ yields the following evolution equation for the radius function $R := R(t)$,

$$\zeta(R, \theta_0, \theta_1)\dot{R} = -\chi(R, \theta_0, \theta_1), \tag{3.19}$$

where the function $\theta_1 := \theta_1(t)$ is updated according to Eq. (3.1). This ODE (3.19) governs the interface evolution of a retracting semi-infinite thin film depicted by Fig. 1; this is a reduced-order variational model for the dewetting of a solid film on a substrate via surface diffusion. Note that we also can treat (3.19) and (3.3) as the coupled ODEs, where they are governed by the two unknown functions θ_1 and R. Numerical methods can be easily applied to solving the coupled ODEs.

4. Asymptotic analysis and numerical verification

We first perform an asymptotic analysis of the ODE (i.e., Eq. (3.19)) to obtain a simple, power-law description of dewetting. For simplicity of presentation, we focus on the special case of $\theta_0 = \pi/2$. Numerical results

are presented for other Young's angles below. For $\theta_0 = \pi/2$, the expressions for $\chi(R, \theta_0, \theta_1)$ defined as (3.10) and $\zeta(R, \theta_0, \theta_1)$ in Eq. (3.19) can be simplified. Inserting Eqs. (3.3) and (3.8) into Eq. (3.10) gives

$$-\chi(R, \theta_0, \theta_1) = -\gamma_0 \Big\{ \frac{1}{\cos\theta_1} \Big[(\frac{\pi}{2} + \theta_1)(\cos\theta_1 - 1) - \sin\theta_1 \cos\theta_1 \Big] + \frac{1}{\sin\theta_1}(1 - \cos\theta_1)\cos\theta_1 \Big\}. \tag{4.1}$$

The expression $\zeta(R, \theta_0, \theta_1)$ in Eq. (3.17) simplifies by rewriting $g_3 = -(\pi/2 + \theta_1)\cos\theta/\cos\theta_1 + \theta + \pi/2$ and

$$\begin{aligned} \int_{-\theta_0}^{\theta_1} g_3(\theta, \frac{\pi}{2}, \theta_1)^2 \, \mathrm{d}\theta &= \frac{1}{2}\Big(\frac{\theta_1 + \pi/2}{\cos\theta_1}\Big)^2 \Big(\frac{\pi}{2} + \theta_1 + \sin\theta_1\cos\theta_1\Big) + \frac{1}{3}\Big(\theta_1 + \frac{\pi}{2}\Big)^3 \\ &\quad -2\Big(\frac{\theta_1 + \pi/2}{\cos\theta_1}\Big)\Big(\frac{\pi}{2}\sin\theta_1 + \theta_1\sin\theta_1 + \cos\theta_1\Big). \end{aligned} \tag{4.2}$$

In the long-time limit, we can assume $R \gg h_0$ such that $\cos\theta_1 = h_0/R \ll 1$. This implies that $\theta_1 \approx \pi/2 + \mathcal{O}(h_0/R)$ and $\sin\theta_1 \approx 1 + \mathcal{O}((h_0/R)^2)$. With these approximations, Eq. (4.1) reduces to

$$\begin{aligned} -\chi(R, \theta_0, \theta_1) &= -\gamma_0 \Big[\Big(\frac{R}{h_0}\Big)\Big(\Big[\pi + \mathcal{O}\Big(\frac{h_0}{R}\Big)\Big]\Big(\frac{h_0}{R} - 1\Big) - \Big[1 + \mathcal{O}\Big(\frac{h_0}{R}\Big)^2\Big]\frac{h_0}{R}\Big) + \frac{1 - h_0/R}{1 + \mathcal{O}((h_0/R)^2)}\Big(\frac{h_0}{R}\Big)\Big] \\ &\approx \pi\gamma_0\Big(\frac{R}{h_0}\Big), \end{aligned} \tag{4.3}$$

where in the last line we keep only the leading order term. In the same limit, Eq. (4.2) reduces to

$$\begin{aligned} \int_{-\theta_0}^{\theta_1} g_3(\theta, \theta_0, \theta_1)^2 \, \mathrm{d}\theta &= \frac{1}{2}\Big[\pi + \mathcal{O}\Big(\frac{h_0}{R}\Big)^2\Big]\Big(\frac{R}{h_0}\Big)^2\Big(\pi + \mathcal{O}\Big(\frac{h_0}{R}\Big) + \Big[1 + \mathcal{O}\Big(\Big(\frac{h_0}{R}\Big)^2\Big)\Big]\frac{h_0}{R}\Big) \\ &\quad -2\Big[\pi + \mathcal{O}\Big(\frac{h_0}{R}\Big)\Big]\Big(\frac{R}{h_0}\Big)\Big(\frac{\pi}{2}\Big[1 + \mathcal{O}\Big(\Big(\frac{h_0}{R}\Big)^2\Big)\Big] \\ &\quad + \Big[\frac{\pi}{2} + \mathcal{O}\Big(\frac{h_0}{R}\Big)\Big]\Big(1 + \mathcal{O}\Big(\Big(\frac{h_0}{R}\Big)^2\Big) + \frac{h_0}{R}\Big) + \frac{1}{3}\Big(\pi + \mathcal{O}(\frac{h_0}{R})\Big)^3 \\ &\approx \frac{\pi^3}{2}\Big(\frac{R}{h_0}\Big)^2. \end{aligned}$$

Inserting this expression into Eq. (3.17), we obtain

$$\zeta(R, \frac{\pi}{2}, \theta_1) \approx \frac{\pi^3 k_B T}{2 D_s \nu \Omega_0^2 h_0^2} R^5.$$

Finally, by inserting this expression and Eq. (4.3) into the ODE describing dewetting Eq. (3.19), we obtain a simplified (leading-order) ODE for dewetting:

$$R^4 \dot{R} = a, \tag{4.4}$$

where $a = 2B\gamma_0 h_0/\pi^2$ and $B = D_s \nu \Omega_0^2 / k_B T$ is a material constant.

Eq. (4.4) demonstrates that

$$R(t) = (5at + C_1)^{1/5} \propto (5a)^{1/5} \, t^{1/5},$$

where C_1 is a constant that depends on the initial value of R. This implies that the ridge adjacent to the moving contact grows with time in a power law fashion as $t^{1/5}$. This power-law exponent is consistent with the previous analysis [15,22,32] and experimental observations [1,30].

Next, we examine how the contact point $x_c := x_c(t)$ moves at long time. The contact point evolution is related to $R(t)$ by

$$x_c(t) = x_0(t) - R(t)\sin\theta_0 = x_0(t) - R(t), \tag{4.5}$$

then by taking the time derivative and using Eq. (3.7), we obtain

$$\dot{x_c} = (g_2 - 1)\dot{R}. \tag{4.6}$$

Eq. (3.8) implies

$$g_2 - 1 = \frac{1}{\cos\theta_1}\Big(\frac{\pi}{2} + \theta_1\Big) - 1 = \Big(\frac{h_0}{R}\Big)^{-1}\Big(\pi + \mathcal{O}\big(\frac{h_0}{R}\big)\Big) - 1 \approx \pi\Big(\frac{h_0}{R}\Big)^{-1} = \frac{\pi R}{h_0}, \tag{4.7}$$

such that, in the long-time limit (i.e., to leading-order),

$$\dot{x_c} = \frac{\pi R}{h_0}\dot{R}. \tag{4.8}$$

Integration of this expression leads to

$$x_c(t) = \frac{\pi R^2(t)}{2h_0} + C_2 \propto b\, t^{2/5}, \tag{4.9}$$

where C_2 is also a constant determined by the initial location of the contact point and $b^5 = (5B\gamma_0)^2\pi/(2h_0)^3$. This is consistent with earlier results for the power-law dependence of the retraction distance with time in the solid-state dewetting [15,19,21,22,30].

The coupled ODEs, Eqs. (3.19)-(3.3), can be solved numerically for all times. We employ the classical fourth-order Runge-Kutta method for any initial conditions and Young's angle, θ_0. Here, because our main focus is on the power-law scaling of surface diffusion-controlled, solid-state dewetting kinetics. for simplicity, we examine the initial values (e.g., $R(0) = 2h_0$ and $\theta_1(0) = \pi/16$) under different isotropic Young's angles. Note that although the initial values of R and θ_1 may not be consistent with Eq. (3.1), they will quickly become consistent after a short time of evolution.

Figures 2 and 3 show numerical results for the evolution of the ridge radius and contact retraction velocity for six different isotropic Young's angles $\theta_0 = 15°$, $30°$, $60°$, $90°$, $120°$ and $150°$. As shown in Fig. 2, a log-log plot of the ridge radius R *versus* time clearly exhibits a $1/5$ power-law at late times for all six different Young's angles. The ridge height (i.e., $R + y_0 = R(1 - \cos\theta_0)$) also follows the same power-law during dewetting. Figure 3 shows that the contact retraction velocity $\dot{x}_c$ is consistent with the predicted power-law $\dot{x}_c \propto t^{-3/5}$ at late times, which indicates that the retraction distance $x_c(t)$ satisfies a $2/5$ power-law with time.

5. Derivation and numerical simulations for a full model

In this section, we derive another dimensionless model based on the OVP to simulate surface diffusion-controlled solid-state dewetting. We first consider a smooth surface for the solid thin film. Suppose the surface is described by a half-open curve $\Gamma := \Gamma(t)$ in 2D with a contact point $x_c := x_c(t)$ moving along the substrate. *For simplicity, we consider the non-dimensionalized problem in this section.* The total interfacial energy is defined by:

$$W = |\Gamma(t)| + \sigma x_c, \tag{5.1}$$

where $\sigma := \cos\theta_0 = \frac{\gamma_{VS} - \gamma_{FS}}{\gamma_0}$. Notice that $|\Gamma(t)|$ is infinite large as the profile is semi-infinite on the right-hand side. We select a point (x_r, h_0) where $x_r \gg x_c$, so that the distance from this point to the contact point is large enough to simulate the semi-infinite profile. Denote $\mathbf{X} := \mathbf{X}(s,t) = (x(s,t), y(s,t))$ as the parameterization of $\Gamma(t)$, where s is the arc length along the interface, t is the time, $\kappa := \kappa(s,t)$ is the curvature of the interface curve, and $L(t) := |\Gamma(t)|$ is the total length of the curve. We impose the following boundary conditions on the thin film [15,19,21]:

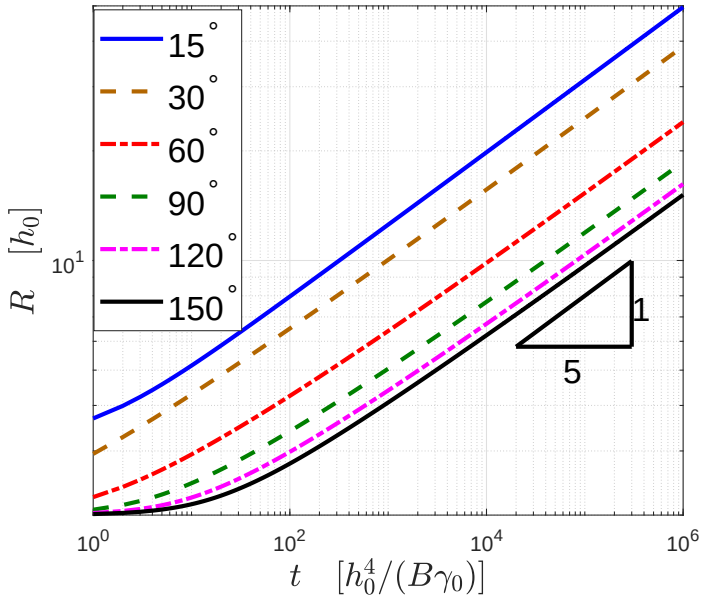

Figure 2: The ridge radius R (i.e., proportional to ridge height) versus time t for six different Young's angles $\theta_0 = 15°$, $30°$, $60°$, $90°$, $120°$, and $150°$. The late time data is consistent with a power-law of the form $R \propto t^{1/5}$ for all Young's angles.

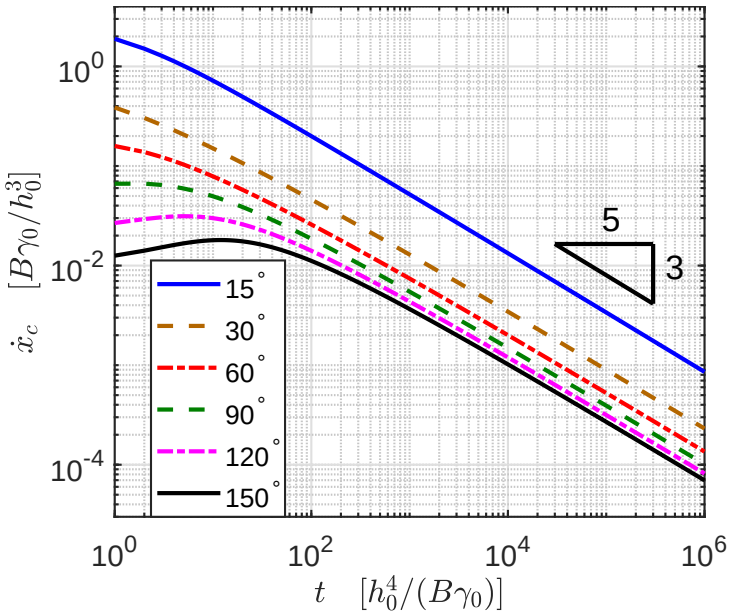

Figure 3: The retraction velocity of the contact point $\dot{x}_c$ *versus* time t for the same six Young's angles as in Fig. 2, where a power law that $\dot{x}_c \propto t^{-3/5}$ is clearly shown. The late time data is consistent with a power-law of the form $x_c \propto t^{2/5}$ for all Young's angles.

(i) Contact point condition

$$y(0,t)=0, \quad y(L(t),t)=h_0, \quad t\geq 0, \tag{5.2}$$

(ii) Fixed contact angle condition

$$\cos\theta^l-\sigma=0, \quad \dot{x}_r=0, \quad t\geq 0, \tag{5.3}$$

(iii) Zero-mass flux condition

$$\partial_s\kappa(0,t)=0, \quad \partial_s\kappa(L(t),t)=0, \quad t\geq 0. \tag{5.4}$$

where $\theta^l:=\theta^l(t)$ is the contact angle at the left contact point and h_0 is the thickness of the semi-infinite film. Here, we assume that the velocity of the "right endpoint" (x_r,h_0) is always zero because it is far enough from the contact point $x_c(t)$.

The time derivative of the surface energy W is easily obtained as (see [21,45,47]):

$$\frac{dW}{dt}=-(\cos\theta^l-\sigma)\dot{x}_c+\int_{\Gamma(t)}v_n\kappa\,ds. \tag{5.5}$$

The dissipation function is formulated by:

$$\Phi=\frac{1}{2}\int_{\Gamma(t)}J^2\,ds. \tag{5.6}$$

Here, J is the mass flux satisfying the conservation condition $v_n+\partial_s J=0$. We introduce a Lagrange multiplier λ for the mass-conservation condition and define the Rayleighian by:

$$\begin{aligned}\mathcal{R}(\dot{\mathbf{X}},\lambda,J)=&\Phi+\dot{W}+\int_\Gamma\lambda(s)(\partial_s J+\mathbf{X}_t\cdot\mathbf{n})ds\\ =&\Phi+\dot{W}-\int_\Gamma\big(J\partial_s\lambda(s)-\lambda(s)\mathbf{X}_t\cdot\mathbf{n}\big)ds\\ =&\Phi+\dot{W}+\mathcal{L},\end{aligned} \tag{5.7}$$

where we use the zero-mass flux condition, and $\mathcal{L}:=-\int_\Gamma\big(J\partial_s\lambda(s)-\lambda(s)\mathbf{X}_t\cdot\mathbf{n}\big)ds$ represents the energy contribution in the Rayleighian from the Lagrange multiplier.

By taking variations of $\mathcal{R}$ with respect to $\mathbf{X}_t,\lambda,J,\dot{x}_c$, we obtain:

$$\frac{\delta\mathcal{R}}{\delta\mathbf{X}_t}=\kappa\mathbf{n}+\lambda\mathbf{n}=0, \tag{5.8}$$

$$\frac{\delta\mathcal{R}}{\delta J}=J-\partial_s\lambda=0, \tag{5.9}$$

$$\frac{\delta\mathcal{R}}{\delta\lambda}=\partial_s J+\mathbf{X}_t\cdot\mathbf{n}=0, \tag{5.10}$$

$$\frac{\delta\mathcal{R}}{\delta\dot{x}_c}=-(\cos\theta^l-\sigma)-L(t)\lambda(0)n^1(0)\dot{x}_c=0, \tag{5.11}$$

with the boundary condition

$$y(0,t)=0, \quad y(L(t),t)=h_0, \quad x_r(t)=x_r(0), \quad J(0,t)=J(L(t),t)=0. \tag{5.12}$$

This leads to a partial differential equation model for the solid thin film.

In the following, we will use the OVP to derive a discrete model by approximating the surface Γ using piecewise linear curves. Let $\mathbf{X}_i:=\mathbf{X}_i(t)=(x_i(t),y_i(t))$ be the vertices of the piecewise linear curves Γ^h (see

Figure 4), and J_i, $i = 1, \ldots, N$, be the flux at these points, respectively. We derive a discrete model that can be solved numerically.

We discretize the dissipation function and the free energy using proper quadratures to compute the discrete Rayleighian. Denote $L_i = |\mathbf{X}_{i+1} - \mathbf{X}_i|$ as the arc length of the i-th segment. Then the discrete Rayleighian $\mathcal{R}^h$ is given by:

$$\mathcal{R}^h = \Phi^h + \dot{W}^h + \mathcal{L}^h, \tag{5.13}$$

where

$$\Phi^h = \frac{1}{2}\sum_{i=1}^{N-1} J_i^2 L_i, \tag{5.14a}$$

$$W^h = \sum_{i=1}^{N-1} L_i + \sigma x_1, \tag{5.14b}$$

$$\mathcal{L}^h = \sum_{i=1}^{N-1} -J_i(\lambda_{i+1} - \lambda_i) + \frac{1}{2}\sum_{i=1}^{N-1} \left(\lambda_i \dot{\mathbf{X}}_i + \lambda_{i+1}\dot{\mathbf{X}}_{i+1}\right) \cdot \mathbf{n}_i L_i, \tag{5.14c}$$

where $\mathbf{n}_i$ is the unit outer normal vector of the segment $(\mathbf{X}_i, \mathbf{X}_{i+1})$:

$$\mathbf{n}_i = -[\partial_s \mathbf{X}]^{\perp}\big|_{\mathbf{X}=\mathbf{X}_i} = \frac{(-(y_{i+1} - y_i), x_{i+1} - x_i)^T}{L_i}. \tag{5.15}$$

By taking derivatives with respect to $\dot{\mathbf{X}}_i, \lambda_i, J_i$, $i = 2, \ldots, N-1$, we obtain

$$\frac{\partial \mathcal{R}^h}{\partial J_i} = J_i L_i - (\lambda_{i+1} - \lambda_i) = 0, \tag{5.16a}$$

$$\frac{\partial \mathcal{R}^h}{\partial \lambda_i} = J_i - J_{i-1} + \frac{1}{2}\left(\mathbf{n}_i L_i + \mathbf{n}_{i-1} L_{i-1}\right) \cdot \dot{\mathbf{X}}_i = 0, \tag{5.16b}$$

$$\frac{\partial \mathcal{R}^h}{\partial \dot{\mathbf{X}}_i} = \frac{\mathbf{X}_i - \mathbf{X}_{i+1}}{L_i} + \frac{\mathbf{X}_i - \mathbf{X}_{i-1}}{L_{i-1}} + \frac{1}{2}\left(\mathbf{n}_i L_i + \mathbf{n}_{i-1} L_{i-1}\right)\lambda_i = 0. \tag{5.16c}$$

The boundary conditions are formulated as:

$$\frac{\partial \mathcal{R}^h}{\partial \dot{x}_c} = \frac{x_c - x_2}{L_1} + \sigma + \frac{1}{2}\mathbf{n}_1^{(1)} L_1 \lambda_1 = 0, \tag{5.17}$$

$$y_1 = 0, \quad y_N = h_0, \quad x_r(t) = x_r(0), \quad J_1 = J_N = 0. \tag{5.18}$$

Equation (5.16) is a system of differential algebraic equations. We further use the backward Euler method to discretize the time derivative $\dot{\mathbf{X}}$ and adopt a semi-implicit technique for nonlinear terms. This leads to the fully discrete scheme below:

$$J_i^{m+1} L_i^m - (\lambda_{i+1}^{m+1} - \lambda_i^{m+1}) = 0, \qquad i = 2, \ldots, N-1, \tag{5.19a}$$

$$\tau(J_i^{m+1} - J_{i-1}^{m+1}) + \frac{1}{2}\left(\mathbf{n}_i^m L_i^m + \mathbf{n}_{i-1}^m L_{i-1}^m\right) \cdot \left(\mathbf{X}_i^{m+1} - \mathbf{X}_i^m\right) = 0, \qquad i = 2, \ldots, N-1, \tag{5.19b}$$

$$\frac{\mathbf{X}_i^{m+1} - \mathbf{X}_{i+1}^{m+1}}{L_i^m} + \frac{\mathbf{X}_i^{m+1} - \mathbf{X}_{i-1}^{m+1}}{L_{i-1}^m} + \frac{1}{2}\left(\mathbf{n}_i^m L_i^m + \mathbf{n}_{i-1}^m L_{i-1}^m\right)\lambda_i^{m+1} = 0, \qquad i = 2, \ldots, N-1, \tag{5.19c}$$

coupled with the boundary conditions

$$\frac{x_c^{m+1} - x_2^{m+1}}{L_1^m} + \sigma + \frac{1}{2}\mathbf{n}_1^{(1)} L_1^m \lambda_1^{m+1} = 0, \quad y_1^{m+1} = 0, \quad y_N^{m+1} = h_0, \quad x_r^{m+1} = x_r^0, \quad J_1^{m+1} = J_N^{m+1} = 0. \tag{5.20a}$$

We remark here that, for the above numerical scheme, the evolution interface profile is discretely approximated by the polygonal curve, i.e., the position of vertices of the polygon $\mathbf{X}_i, i = 1, \ldots, N$, and they are slow variables we choose in this section in order to describe the interface evolution. Based on the discrete approximation, we can rewrite the total free energy function and dissipation function as a function of $\mathbf{X}_i$ and its velocity $\dot{\mathbf{X}}_i$, $i = 1, \ldots, N$. Based on OVP, we then derive the ODEs governing the temporal evolution of the slow variables $\mathbf{X}_i$ so that the evolution of thin film can be tracked by solving these ODEs. This method does not need to beforehand know the dynamic PDEs which describe the evolution of the system. The core idea of the method lies in designing the free energy and dissipation function as a function of the interested slow variables, thereby directly deriving the discrete governing equations based on OVP. Similar ideas can be applied to some more complicatied systems, e.g., in fluid mechanics and soft matter.

In the following, we present several numerical results for a thin film with different contact angles by solving the system (5.19)-(5.20). Figures 4 and 5 show the early-time profiles of the film surface for $\theta_0 = 60°$ and $120°$, respectively. The "peak" and "valley" structures gradually appear as time evolves. We solve the problem for a sufficiently long time until the valley touches the substrate and a pinch-off occurs. Figures 6 and 7 show the profiles of the thin film at the moment of pinch-off for six different isotropic Young's angles $\theta_0 = 30°$, $60°$, $90°$, $120°$, $150°$ and $180°$, respectively. As shown in Figures 6 and 7, as the contact angle decreases, the pinch-off time increases, and the location of the breakup moves farther away from the left contact point.

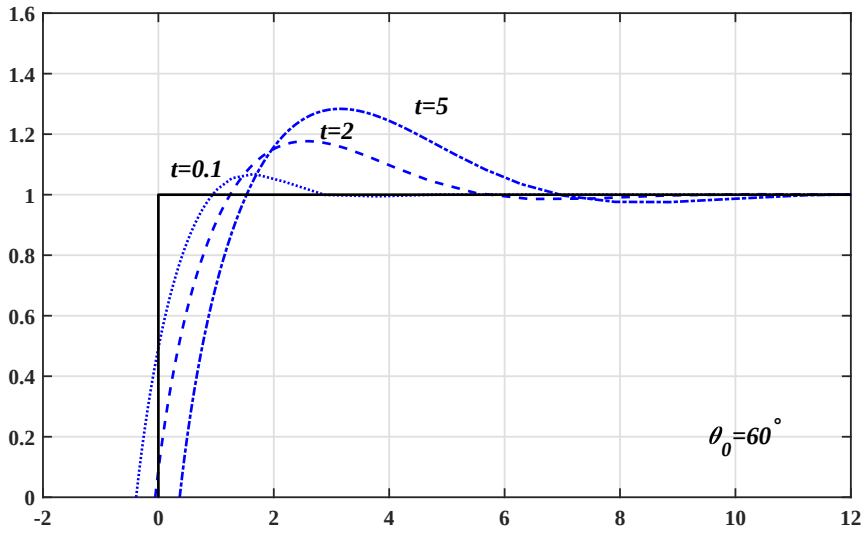

Figure 4: Early-time profiles of the film-vapor interface for $\theta_0 = 60°$.

Figure 8 shows numerical results for the evolution of the contact point, the peak thickness, and the valley thickness for the six different isotropic Young's angles $\theta_0 = 30°$, $60°$, $90°$, $120°$, $150°$ and $180°$, respectively. As shown in Fig. 8(a), the evolution of the retraction distance $x_c(t)$ follows a power law $x_c \propto t^{2/5}$ at late times, which indicates a $-3/5$ power-law for the contact retraction velocity $\dot{x}_c$. As shown in Fig. 8(b), a log-log plot of the ridge height $H_{\max}$ versus time clearly exhibits a $1/5$ power-law at late times for all six Young's angles. More precisely, we compute the power-law exponent by performing a linear fit on the log-log plots of x_c and $H_{\max}$ and calculating the slope of the fitting line. The results are listed in Tables 1 and 2. We clearly observe

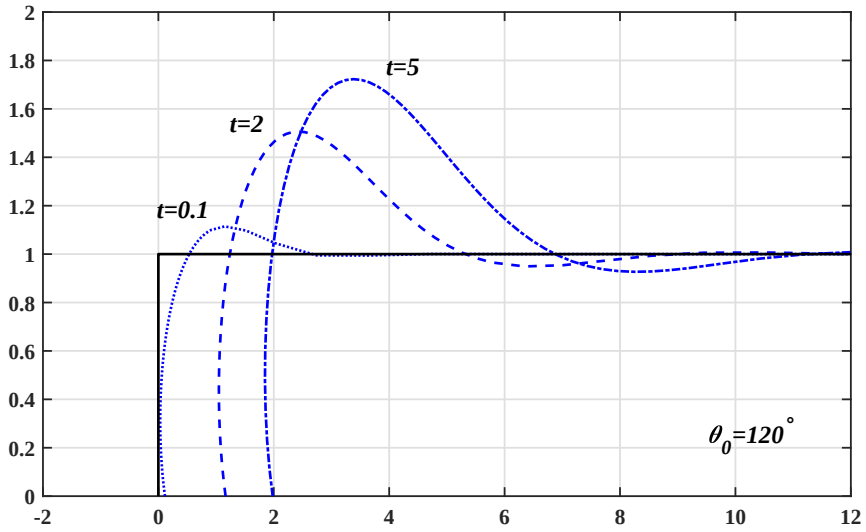

Figure 5: Early-time profiles of the film-vapor interface for $\theta_0 = 120°$.

that the slopes of the fitting lines for x_c and $H_{\max}$ approach $\frac{2}{5}$ and $\frac{1}{5}$, respectively, as the mesh is refined. The numerical results are in good agreement with the analytical results predicted by the reduced model in the previous section.

	$\theta_0 = 30°$	$\theta_0 = 60°$	$\theta_0 = 90°$	$\theta_0 = 120°$	$\theta_0 = 150°$	$\theta_0 = 180°$
$N = 15$	0.466	0.434	0.424	0.421	0.418	0.417
$N = 40$	0.421	0.421	0.420	0.418	0.414	0.411
$N = 100$	0.423	0.420	0.418	0.415	0.409	0.404

Table 1: Slope of the linear fitting line on the log-log plots of x_c and t for different mesh sizes N under different Young contact angles θ_0.

	$\theta_0 = 30°$	$\theta_0 = 60°$	$\theta_0 = 90°$	$\theta_0 = 120°$	$\theta_0 = 150°$	$\theta_0 = 180°$
$N = 15$	0.160	0.162	0.153	0.156	0.167	0.171
$N = 40$	0.205	0.172	0.204	0.213	0.197	0.185
$N = 100$	0.215	0.194	0.184	0.192	0.193	0.192

Table 2: Slope of the linear fitting line on the log-log plots of $H_{\max}$ and t for different mesh sizes N under different Young contact angles θ_0.

Finally, we performed numerical simulations to investigate whether this pinch-off behavior has any scaling property. Indeed, we found that there exists a power law scaling between $H_{\min}$ and $(t^* - t)^\alpha$ according to our numerical results, where t^* is the pinch-off time. As shown in Figure 9, it can be found that the power law satisfies $\alpha \approx 1$, where we applied the least square linear fitting for the log-log plot of $H_{\min}$. Furthermore, Figure 10 illustrates the bahavior of $H_{\min}$ versus the rescaled time t/t^*, and we can also observe that the evolution curve of the valley thickness $H_{\min}$ remains almost the same regardless of the different contact angles θ_0.

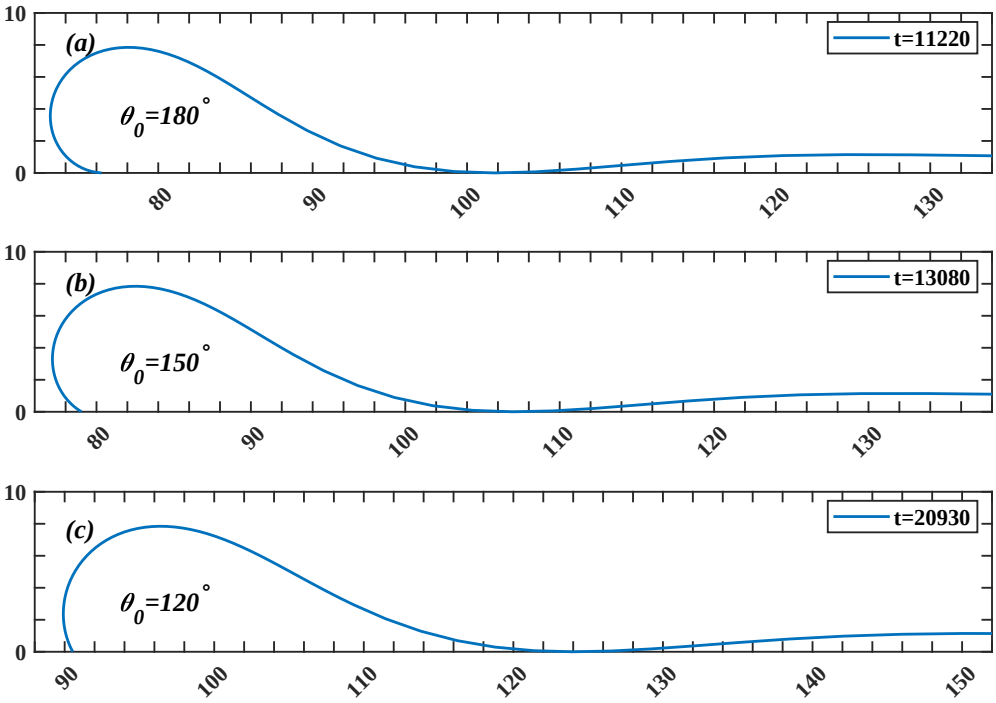

Figure 6: Film profile at the moment of pinch-off for contact angles $\theta_0 = 120°, 150°, 180°$.

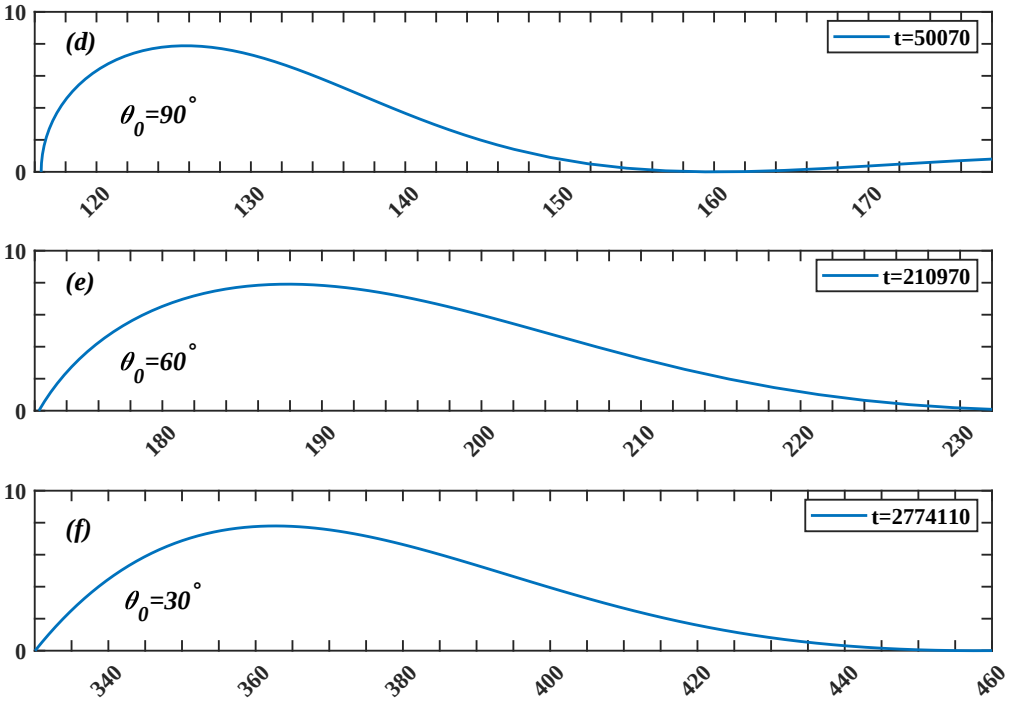

Figure 7: Film profile at the moment of pinch-off for contact angles $\theta_0 = 30°, 60°, 90°$.

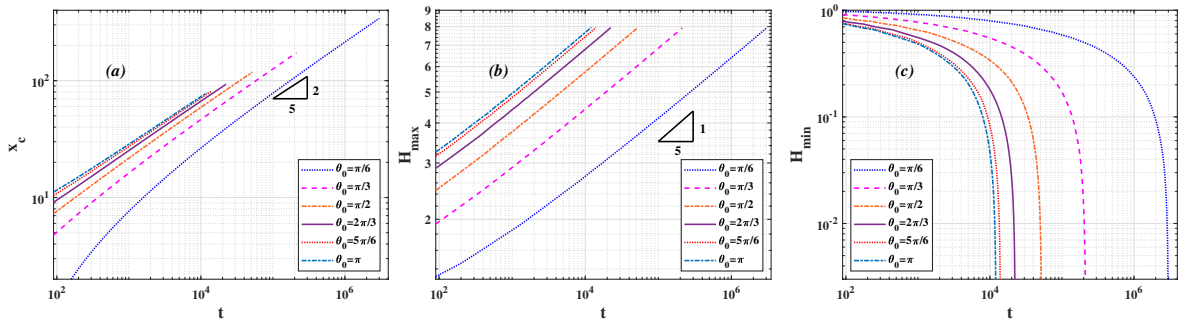

Figure 8: Geometric quantities versus time t for six different Young's angles $\theta_0 = 30°$, $60°$, $90°$, $120°$, $150°$ and $180°$: (a) Retraction distance $x_c(t)$ versus time; (b) Ridge height $H_{\max}$ versus time; (c) Minimum height $H_{\min}$ (i.e., the height of the "valley") versus time.

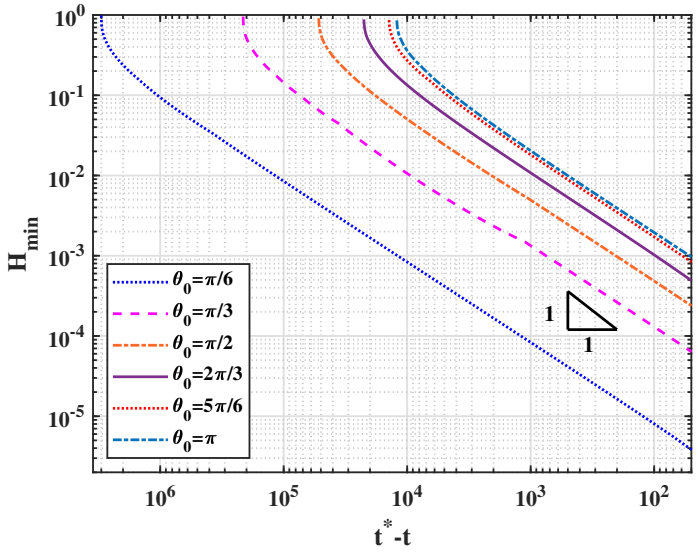

Figure 9: Minimum height $H_{\min}$ versus $t^* - t$ under six different Young?s angles $\theta_0 = 30°, 60°, 90°, 120°, 150°$ and $180°$, where t^* represents the pinch-off time.

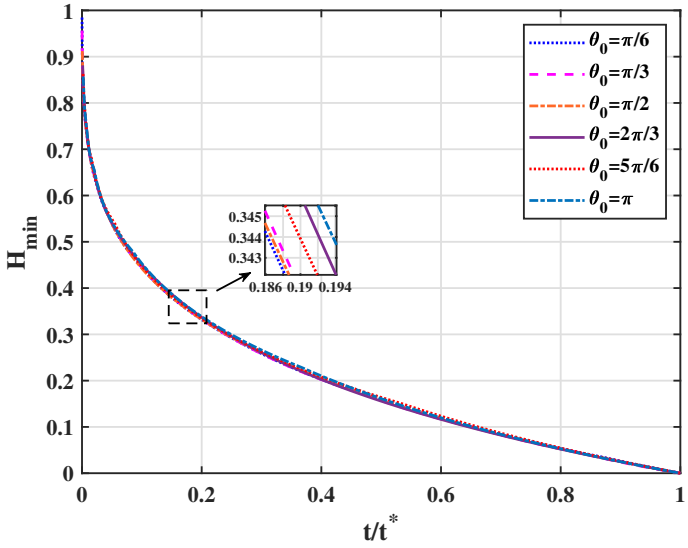

Figure 10: Minimum height $H_{\min}$ versus the rescaled time t/t^* under six different Young?s angles $\theta_0 = 30°, 60°, 90°, 120°, 150°$ and $180°$, where t^* represents the pinch-off time.

6. Conclusions

We examine the power-law scaling of the surface diffusion-controlled, solid-state dewetting of a semi-infinite thin film on a flat substrate. Our approach is based upon the OVP and motivated by earlier, simple geometric models that are consistent with the power-law retraction behavior observed in more complete numerical studies of the evolving film profile during solid-state dewetting. The simplified nature of the film geometry allows us to derive a reduced-order variational model, the evolution of which is governed by an ODE. Asymptotic analysis and numerical simulations of the ODE reproduce the 2/5 power-law of the retraction distance with time, and the 1/5 time exponent for the height of the ridge adjacent to the moving contact line. We also present a numerical model based on the OVP to study not only power-laws, but also the profile of the thin film. The numerical results have good agreements with those predicted by the reduced-order model. Although these power-laws have been predicted previously based on analysis and numerical simulation, the present results demonstrate the simplicity and applicability of the OVP to describe surface diffusion-controlled morphology evolution problems in materials science. While the geometric model employed here is very simple, the OVP approach is applicable to much more complex representations of the geometry; such generalizations yield a more complicated system of ODEs.

Data availability statement

No data was used for the research described in the article.

Acknowledgement

W. Jiang was partially supported by the National Natural Science Foundation of China (No. 12271414) and the Guangdong Basic and Applied Basic Research Foundation (No. 2024A1515012505). X. Xu was partially supported by the National Natural Science Foundation of China (No. 12371415, 12461160275), and by the Beijing Natural Science Foundation (No. Z240001).

Declaration of competing interest

The authors declare that they have no known competing financial interests or personal relationships that could have appeared to influence the work reported in this paper.

References

[1] C. V. Thompson, Solid-state dewetting of thin films, Annu. Rev. Mater. Res. 42 (2012) 399–434.

[2] E. Jiran, C. V. Thompson, Capillary instabilities in thin films, J. Electron. Mater. 19 (11) (1990) 1153–1160.

[3] O. Pierre-Louis, A. Chame, Y. Saito, Dewetting of ultrathin solid films, Phys. Rev. Lett. 103 (19) (2009) 195501.

[4] J. Ye, C. V. Thompson, Regular pattern formation through the retraction and pinch-off of edges during solid-state dewetting of patterned single crystal films, Phys. Rev. B 82 (19) (2010) 193408.

[5] J. Ye, C. V. Thompson, Templated solid-state dewetting to controllably produce complex patterns, Adv. Mater. 23 (13) (2011) 1567–1571.

[6] F. Leroy, F. Cheynis, Y. Almadori, S. Curiotto, M. Trautmann, J. Barbé, P. Müller, et al., How to control solid state dewetting: A short review, Surface Science Reports 71 (2) (2016) 391–409.

[7] O. Kovalenko, S. Szabó, L. Klinger, E. Rabkin, Solid state dewetting of polycrystalline Mo film on sapphire, Acta Mater. 139 (2017) 51–61.

[8] M. Naffouti, R. Backofen, M. Salvalaglio, T. Bottein, M. Lodari, A. Voigt, T. David, A. Benkouider, I. Fraj, L. Favre, et al., Complex dewetting scenarios of ultrathin silicon films for large-scale nanoarchitectures, Science Advances 3 (11) (2017) eaao1472.

[9] L. Armelao, D. Barreca, G. Bottaro, A. Gasparotto, S. Gross, C. Maragno, E. Tondello, Recent trends on nanocomposites based on Cu, Ag and Au clusters: A closer look, Coord. Chem. Rev. 250 (11) (2006) 1294–1314.

[10] J. Mizsei, Activating technology of SnO_2 layers by metal particles from ultrathin metal films, Sensors and Actuators B: Chemical 16 (1) (1993) 328–333.

[11] S. Rath, M. Heilig, H. Port, J. Wrachtrup, Periodic organic nanodot patterns for optical memory, Nano Lett. 7 (12) (2007) 3845–3848.

[12] S. Randolph, J. Fowlkes, A. Melechko, K. Klein, H. Meyer III, M. Simpson, P. Rack, Controlling thin film structure for the dewetting of catalyst nanoparticle arrays for subsequent carbon nanofiber growth, Nanotechnology 18 (46) (2007) 465304.

[13] V. Schmidt, J. V. Wittemann, S. Senz, U. Gösele, Silicon nanowires: a review on aspects of their growth and their electrical properties, Adv. Mater 21 (25-26) (2009) 2681–2702.

[14] D. J. Srolovitz, S. A. Safran, Capillary instabilities in thin films: II. Kinetics, J. Appl. Phys. 60 (1) (1986) 255–260.

[15] H. Wong, P. Voorhees, M. Miksis, S. Davis, Periodic mass shedding of a retracting solid film step, Acta Mater. 48 (8) (2000) 1719–1728.

[16] E. Dornel, J. Barbe, F. De Crécy, G. Lacolle, J. Eymery, Surface diffusion dewetting of thin solid films: Numerical method and application to Si/SiO_2, Phys. Rev. B 73 (11) (2006) 115427.

[17] E. Bussmann, F. Cheynis, F. Leroy, P. Müller, O. Pierre-Louis, Dynamics of solid thin-film dewetting in the silicon-on-insulator system, New J. Phys. 13 (4) (2011) 043017.

[18] M. Dufay, O. Pierre-Louis, Anisotropy and coarsening in the instability of solid dewetting fronts, Phys. Rev. Lett. 106 (10) (2011) 105506.

[19] W. Jiang, W. Bao, C. V. Thompson, D. J. Srolovitz, Phase field approach for simulating solid-state dewetting problems, Acta Mater. 60 (15) (2012) 5578–5592.

[20] E. Rabkin, D. Amram, E. Alster, Solid state dewetting and stress relaxation in a thin single crystalline Ni film on sapphire, Acta Mater. 74 (2014) 30–38.

[21] Y. Wang, W. Jiang, W. Bao, D. J. Srolovitz, Sharp-interface model for solid-state dewetting problems with weakly anisotropic surface energies, Phys. Rev. B 91 (2015) 045303.

[22] R. V. Zucker, W. C. Carter, C. V. Thompson, Power-law scaling regimes for solid-state dewetting of thin films, Scripta Mater. 116 (2016) 143–146.

[23] W. Jiang, Y. Wang, Q. Zhao, D. J. Srolovitz, W. Bao, Solid-state dewetting and island morphologies in strongly anisotropic materials, Scripta Mater. 115 (2016) 123–127.

[24] W. Jiang, Y. Wang, D. J. Srolovitz, W. Bao, Solid-state dewetting on curved substrates, Phys. Rev. Mater. 2 (11) (2018) 113401.

[25] W. Jiang, Q. Zhao, T. Qian, D. J. Srolovitz, W. Bao, Application of Onsager's variational principle to the dynamics of a solid toroidal island on a substrate, Acta Mater. 163 (2019) 154–160.

[26] Q. Zhao, W. Jiang, Y. Wang, D. J. Srolovitz, T. Qian, W. Bao, Dynamics of small solid particles on substrates of arbitrary topography, Acta Mater. 281 (2024) 120407.

[27] P.-G. De Gennes, Wetting: statics and dynamics, Rev. Mod. Phys. 57 (3) (1985) 827–863.

[28] A. K. Tripathi, O. Pierre-Louis, Triple-line kinetics for solid films, Phys. Rev. E 97 (2) (2018) 022801.

[29] J. Ye, C. V. Thompson, Anisotropic edge retraction and hole growth during solid-state dewetting of single crystal nickel thin films, Acta Mater. 59 (2) (2011) 582–589.

[30] G. H. Kim, R. V. Zucker, J. Ye, W. C. Carter, C. V. Thompson, Quantitative analysis of anisotropic edge retraction by solid-state dewetting of thin single crystal films, J. Appl. Phys. 113 (4) (2013) 043512.

[31] R. V. Zucker, G. H. Kim, W. C. Carter, C. V. Thompson, A model for solid-state dewetting of a fully-faceted thin film, Comptes Rendus Physique 14 (7) (2013) 564–577.

[32] R. Brandon, F. J. Bradshaw, Royal aircraft establishment technical report, No.66095 (1966).

[33] R. V. Zucker, Capillary-driven shape evolution in solid-state micro-and nano-scale systems, Ph.D. thesis, Massachusetts Institute of Technology (2015).

[34] L. Onsager, Reciprocal relations in irreversible processes. i., Phys. Rev. 37 (4) (1931) 405–426.

[35] L. Onsager, Reciprocal relations in irreversible processes. ii., Phys. Rev. 38 (12) (1931) 2265–2279.

[36] M. Doi, Onsager's variational principle in soft matter, J. Phys. Condens. Matter 23 (28) (2011) 284118.

[37] M. Doi, Soft matter physics, Oxford University Press, 2013.

[38] M. Doi, Onsager principle as a tool for approximation, Chin. Phys. B 24 (020505) (2015) 1674–1056.

[39] X. Xu, Y. Di, M. Doi, Variational method for liquids moving on a substrate, Phys. Fluids 28 (8) (2016) 087101.

[40] X. Man, M. Doi, Ring to mountain transition in deposition pattern of drying droplets, Phys. Rev. Lett. 116 (6) (2016) 066101.

[41] X. Xu, T. Qian, Hydrodynamic boundary conditions derived from Onsager's variational principle, Procedia IUTAM 20 (2017) 144–151.

[42] Y. Di, X. Xu, J. Zhou, M. Doi, Thin film dynamics in coating problems using Onsager principle, Chin. Phys. B 27 (2) (2018) 024501.

[43] X. Xu, Y. Di, M. Doi, A variational analysis for the moving finite element method for gradient flows, Journal of Computational Mathematics 41 (2) (2023) 191–210.

[44] S. Xiao, X. Xu, A moving mesh method for porous medium equation by the Onsager variational principle, Journal of Computational Physics 536 (2025) 114061.

[45] Y. Liu, X. Xu, A variational discretization method for mean curvature flows by the Onsager principle, CSIAM Transactions on Applied Mathematics 6 (1) (2025) 63–95.

[46] S. Wang, W. Jiang, Numerical approximations based on Onsager variational principle for geometricPDEs: H^{-1}-gradient flow, preprint (2026).

[47] S. Wang, Numerical methods for geometric flows based on the Onsager variational principle and their applications, Ph.D. thesis, Wuhan University (2026).

[48] Z. Suo, Motions of microscopic surfaces, Advances in Applied Mechanics 33 (1997) 193–294.